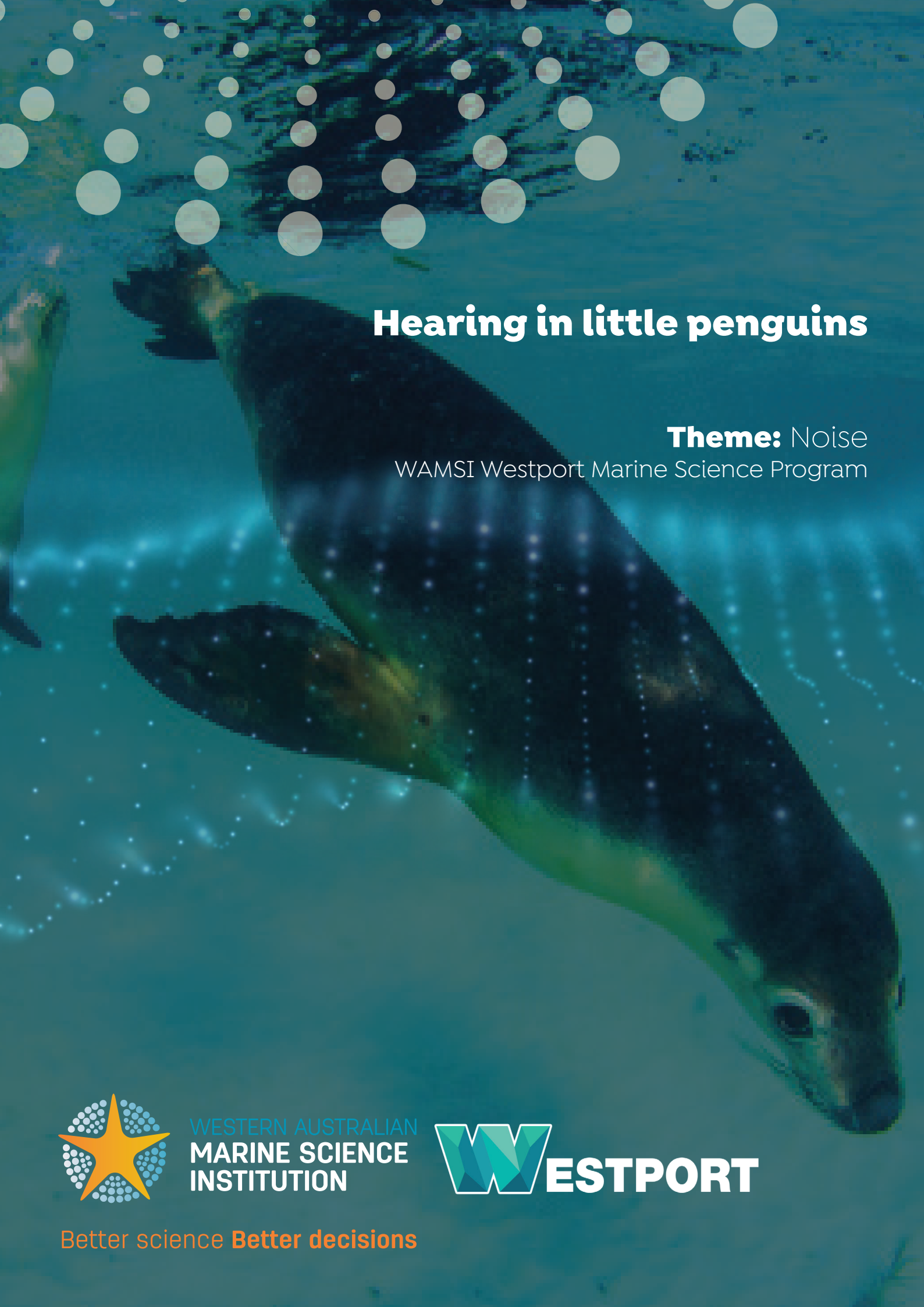

Hearing in little penguins

Theme: Noise

WAMSI Westport Marine Science Program

WESTERN AUSTRALIAN MARINE SCIENCE INSTITUTION

WESTPORT

Better science **Better decisions**

WAMSI WESTPORT MARINE SCIENCE PROGRAM

WESTERN AUSTRALIAN MARINE SCIENCE INSTITUTION

WESTPORT

ABOUT THE MARINE SCIENCE PROGRAM

The WAMSI Westport Marine Science Program (WWMSP) is a $13.5 million body of marine research funded by the WA Government. The aims of the WWMSP are to increase knowledge of Cockburn Sound in areas that will inform the environmental impact assessment of the proposed Westport development and help to manage this important and heavily used marine area into the future. Westport is the State Government's program to move container trade from Fremantle to Kwinana, and includes a new container port and associated freight, road and rail, and logistics. The WWMSP comprises more than 30 research projects in the biological, physical and social sciences that are focused on the Cockburn Sound area. They are being delivered by more than 100 scientists from the WAMSI partnership and other organisations.

FUNDING SOURCES
The $13.5 million WAMSI Westport Marine Science Program was funded by the Western Australian Government, Department of Transport. WAMSI partners provided significant in-kind funding to the program to increase the value to >$22 million.

DATA
Finalised datasets will be released as open data, and data and/or metadata will be discoverable through Data WA and the Shared Land Information Platform (SLIP).

YEAR OF PUBLICATION
August 2024

This report is part of the project: Hearing sensitivity of little penguins.

CITATION
Wei, C., Erbe, C., Cannell, B. (2024). Hearing in little penguins Prepared for the WAMSI Westport Marine Science Program. Western Australian Marine Science Institution, Perth, Western Australia. 28pp.

FRONT COVER IMAGE
Theme: Noise

Contents

The WAMSI Westport Marine Science Program is a $13.5 million body of research that is designed to fill knowledge gaps relating to the Cockburn Sound region. It was developed with the objectives of improving the capacity to avoid, mitigate and offset environmental impacts of the proposed Westport container port development and increase the WA Government's ability to manage other pressures acting on Cockburn Sound into the future. Funding for the program has been provided by Westport (through the Department of Transport) and the science projects are being delivered by the Western Australian Marine Science Institution.

1 Hearing in little penguins

Author/s
Chong Wei, Centre for Marine Science and Technology, Curtin University; chong.wei@curtin.edu.au
Christine Erbe, Centre for Marine Science and Technology, Curtin University; c.erbe@curtin.edu.au
Belinda Cannell, The University of Western Australia; belinda.cannell@uwa.edu.au

Project
Curtin Project Number: RES 64481
CMST Project Number: 1594-5

Executive Summary

In the absence of noise exposure guidelines for marine fauna, a first step in understanding the potential impacts of noise and in designing appropriate noise reduction and mitigation methods is understanding whether the inhabiting animals are sensitive to additional anthropogenic noise sources from port construction and operation. Knowledge of marine fauna's hearing sensitivity is critical to understanding how these aquatic animals, some of which are endangered species, may be affected by anthropogenic noise. An audiogram (i.e., a measure of hearing sensitivity as a function of acoustic frequency) is considered fundamental information for understanding hearing and for assessing noise impacts. However, diving birds, such as penguins, are very difficult to train in aquaria. Currently, no reliable practical methods for measuring audiograms behaviourally or electro-physiologically in this species exist. Therefore, no audiograms for any species of penguins have been measured to-date, neither in air nor under water.

For our research, we collected naturally deceased little penguins (*Eudyptula minor*) for X-ray computed tomography (XCT) and microCT scans. The scan data was used to reconstruct the penguin's head, specifically the ear structures (inner ear, columella, columella's footplate, tympanic membrane, etc.). Two types of 3D finite-element models were built in this research: the full head model based on XCT data and the head with beak removed model based on microCT data (higher resolution). The models simulated the sound reception processes and ear responses to the incident planar waves at the selected frequencies.

The model computed the received sound pressure fields and motion (e.g., displacement, velocity) of the internal ear-related structures. The synergistic response of ear components to incident aerial and underwater sounds at selected frequencies was also calculated. Additionally, the microCT models were used to calculate the in-air and underwater frequency-dependent columella velocity transfer functions between the magnitude of the velocity at the columella's footplate and the amplitude of input sound pressure. The transfer functions were used to predict the in-air and underwater audiograms for the little penguin across a broad frequency range (100 Hz–10 kHz).

Our predicted in-air audiogram showed the lowest threshold (~46 dB re 20 µPa) for the little penguin was at ~2 kHz with a gradual increase in thresholds at lower frequencies and a steeper increase at higher frequencies (>5 kHz). The region of best sensitivity was found at ~550 Hz–5400 Hz. Our predicted underwater audiogram showed that the lowest threshold was at ~83 dB re 1 µPa at ~1.5 kHz. The region of best sensitivity was found at ~200 Hz – 6000 Hz. In general, our predicted in-air and underwater audiograms were comparable with other diving birds in both the form and range of auditory sensitivity. Our predicted in-air audiogram was similar to the data measured in black-footed penguins (*Spheniscus demersus*, also called African penguin) using cochlear potential methods, the

only penguin species for which hearing capability data existed. Our in-air audiograms also fell into the mean range of the measured aerial audiograms of other diving birds. Our predicted underwater audiogram showed a similar frequency-dependent pattern of sensitivity to the data of cormorant fledglings. The slight differences in the curves were likely due to morphological differences among species (e.g., head size and shape). The variability can also be found within the same species from different individuals, depending on sex, age, health, etc. Therefore, modelling more little penguin individuals would be important work for the future to capture the variability in audiograms. It should be noted that we were not able to successfully conduct tissue property measurements due to the small size of little penguins (the maximum length of an adult little penguin is ~30 cm). The parameters of the tissue properties in our model were based on existing literature and knowledge of anatomical similarities, using values from other bird species. Moreover, because of the limitation of the microCT scanner, a full penguin head could not fit into the scanner. Therefore, we removed the beak and placed the incident sound source on the side of the head in the models to avoid the effects of missing the beak. Performing a microCT scan on a full penguin head would be the logical follow-on to this research.

In summary, our research developed a promising method to derive the first in-air and underwater audiograms of the little penguin. The results provide a valuable indication of the ranges of frequencies and levels that can be heard by this species. The outputs from this study can assist efforts in understanding the potential impacts of noise and designing noise reduction and mitigation methods for little penguins, as well as informing environmental impact assessments (EIA) of noise.

2 Introduction

The Australian little penguin (*Eudyptula minor*), also called the fairy penguin, is a species of penguin that only breeds in Australia and New Zealand. Due to various reasons, their numbers are declining at many colonies. Two main concerns potentially causing their decline are food availability (Cannell et al., 2023) and loss of foraging habitat with ambient sounds being an important habitat feature. Previous studies have found that areas exposed to high levels of noise may represent habitat loss for some species, causing a decline in species' presence and density (Bayne et al., 2008). For example, birds (e.g., songbirds) avoid areas with high noise amplitudes (levels) in their habitats (Francis et al., 2012). Research also suggests that noise reduces the quality of seabird habitats, leading to progressively acoustic habitat degradation for seabirds (Slabbekoorn et al., 2018). For instance, noise interferes with the ability to hear predators and other important sounds in the environment (Ortega, 2012). Moreover, many seabirds find food resources through listening (Goerlitz et al., 2008), and so noise could disrupt feeding and cause changes in foraging. Penguins are highly specialised for aquatic life; they dive while travelling and foraging. In some penguins, foraging dives can be as deep and long as in some species of seals at mesopelagic depths. A recent study (Sørensen et al., 2020) has shown that Gentoo penguins (*Pygoscelis papua*) can detect and react to underwater sound, suggesting penguins are likely to make use of sound for orientation and prey detection during dives, and they may be very sensitive to anthropogenic noise (e.g., the noise from ships and near-shore construction). The little penguin spends substantial amounts of time on land as well as in the water engaged in different critical behaviours (e.g., resting and nesting on land, foraging in water) and is thus exposed to potential noise disturbance on land and under water. The little penguin thus is of concern because its critical habitats often overlap with marine areas used by humans for transport, as well as industrial and recreational purposes. However, to date, the lack of information about little penguin sound reception mechanisms and their hearing sensitivity to various acoustic frequencies impedes a thorough assessment of the impacts of anthropogenic noise on these animals. Over the years, only one penguin species, the black-footed/African penguin (*Spheniscus demersus*) has been studied in respect to aerial auditory capabilities by using cochlear potential methods (not auditory thresholds, Wever et al., 1969).

An audiogram represents the auditory hearing thresholds as a function of frequency, which is important information for assessing the potential noise impact. The conventional methods for estimating an audiogram can be classified into three categories: (A) predict an audiogram based on the characteristics of the vocalizations (i.e., what animals can hear, matches what they can generate; Clark, 1990; Matthews et al., 1999); (B) predict an audiogram based on ear anatomy and compare to the functional morphology of ears in well-known closely related species (Ketten, 1994; 1997; 2000); and (C) measure audiogram through practical methods, such as behavioural response experiments and electrophysiological testing (e.g., auditory brainstem response; ABR) (Larsen et al., 2020). Unfortunately, for little penguins, these methods are generally not reliable or practical to extract audiograms from, because this species is more elusive, not easily trainable, and inaccessible for live testing in a well-designed, controlled laboratory condition.

To overcome these challenges, we developed sound reception finite-element (FE) models based on high-resolution computed tomography (CT) imaging. The imaging-based FE modelling techniques allow us to predict audiograms and study the sound reception mechanisms in little penguins. The techniques have been used to study the middle ears of multiple species of terrestrial mammals (Koike et al., 2002; Gan et al., 2004; Homma et al., 2009; 2010; Wang and Gan; 2016; De Greef et al., 2017; Tubelli et al., 2012; 2018). They have also been used to study sound reception and noise impact on multiple marine species, such as fish (Wei et al., 2022), baleen whales (Tubelli et al., 2012; 2018; Cranford and Krysl, 2015), and toothed whales (Aroyan, 2001). The techniques have the advantage of studying the complex acoustic processes when sounds interact with animal biological structures, becoming a useful tool when traditional experimental methods are not available. Based on the audiograms (in-air and underwater), we would be able to assess potential acoustic impacts on little penguins and make relevant mitigation plans, which are critical for conservation efforts.

3 Materials and Methods

3.1 Specimen Collection

We collected three heads of little penguins following their necropsies. The penguins were found at three locations in Western Australia: Mandurah on 8 February 2020 (B200243), Penguin Island on 14 April 2020 (21/0235), and Woodman Point on 23 November 2020 (21/0236). Additionally, three intact bodies of recently deceased little penguins were obtained from Garden Island on 06 June 2019, 24 September 2019, and 21 February 2023 (Figures 1A and B). All the heads of the specimens were intact.

Figure 1. X-ray computed tomography scanning of the little penguins. (A) Two collected little penguin specimens (full body). (B) Three collected little penguin heads. (C) XCT scan of one of the penguins, focusing on its head. (D) XCT scan of the three penguin heads.

3.2 Medical CT Scan and Data Analysis

An accurate FE hearing model requires high-accuracy inputs of geometric information and material properties. We first performed medical CT scanning on all the specimens. Medical CT scanning is a non-destructive technology that provides high-resolution 3D geometry information. We can examine the internal anatomy of animal specimens without the need for dissection by using this method.

The specimens were scanned in 3D by X-ray computed tomography (XCT) using a Siemens SOMATOM definition AS medical scanner installed at the Commonwealth Scientific and Industrial Research Organisation (CSIRO, Curtin Bentley) allowing rapid 3D scanning and that produces XCT transversal images of 128 x 245 pixels (Figures 1C and D). The instrument was calibrated using air and water suitable for organic-based material applications. The scan was conducted using 0.6 mm spiral acquisition and the slice increment was set to 0.1 mm. The energy of the beam was set up to have maximal phase contrast between the different phases of interest (100 kV and 500 mA). The voxel size

(i.e., a pixel in 3D) was set up to allow the entire coverage of the penguin head and was set to 380 µm x 380 µm x 100 µm. The XCT images were reconstructed using two Siemens algorithms: (i) H50s with little noise but less sharp image, and (ii) H70h with granular noise but sharper image, and both stored as DICOM images. The data was then imported into software Horos™ (Horos Project, Geneva, Switzerland) for CT data analysis and geometrical model reconstruction (Figure 2).

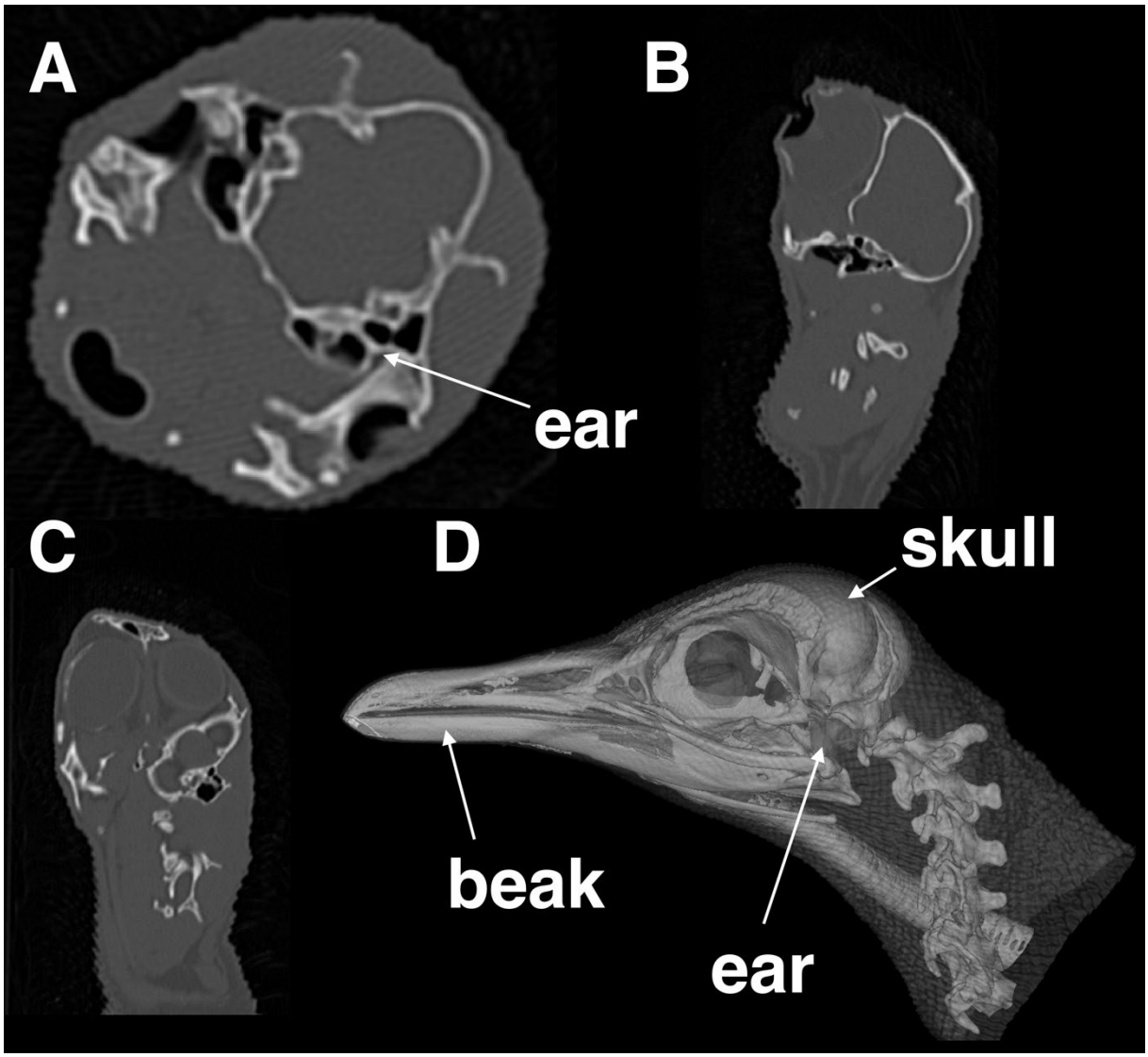

Figure 2. XCT scan of the little penguin's head. (A) Cross plane, (B) frontal plane, and (C) sagittal plane of the head. (D) 3D reconstruction of the head and ear structures. The grey level represents the different Hounsfield unit (HU) values. HU is a dimensionless unit universally used in CT scanning to express CT numbers in a standardized and convenient form. HU values are obtained from a linear transformation of the measured attenuation coefficients.

3.3 Dissection, MicroCT Scan, and Data Analysis

After examining the data (Figure 2), we realised that the resolution of the CT data was not high enough to gain detailed geometric information of the tiny ear structures (i.e., the inner ear, columella, columella's footplate, tympanic membrane, etc.). Therefore, we decided to perform a microCT scan focusing on the ears. Before the microCT scan, we conducted a dissection on one of the penguin heads to study the ear anatomy. Due to the size limitation of the scanner (approximately 40 mm × 40 mm × 40 mm), we had to remove the penguin's beak of the penguin from the head (Figure 3B) without

breaking other structures. Then we fixed the head firmly in a tight plastic container for microCT scanning, as shown in Figures 3C and D.

The microCT scanning was performed at the Australian Resources Research Centre (ARRC, Kensington, Western Australia) using an Xradia VersaXRM-500 microCT scanner. This scanner provides high-resolution 3D X-Ray imaging with submicron resolution. It facilitates non-destructive observation of the internal structure of objects, such as the columella. In the microCT scanning, the isotropic resolution was set as voxel size 29 µm and the power setting was set as 80 kV × 87 µA. The slice increment and slice thickness were both 0.05 mm. Cone-beam reconstruction (Panetta and Camarlinghi, 2020) was performed on the object and the data was saved on a hard drive as a matrix of 1000 x 1024 pixels per image in TIFF format. The images were converted to DICOM format later and imported into the free software Horos™ (Horos Project, Geneva, Switzerland) for data analysis and 3D geometrical model reconstruction.

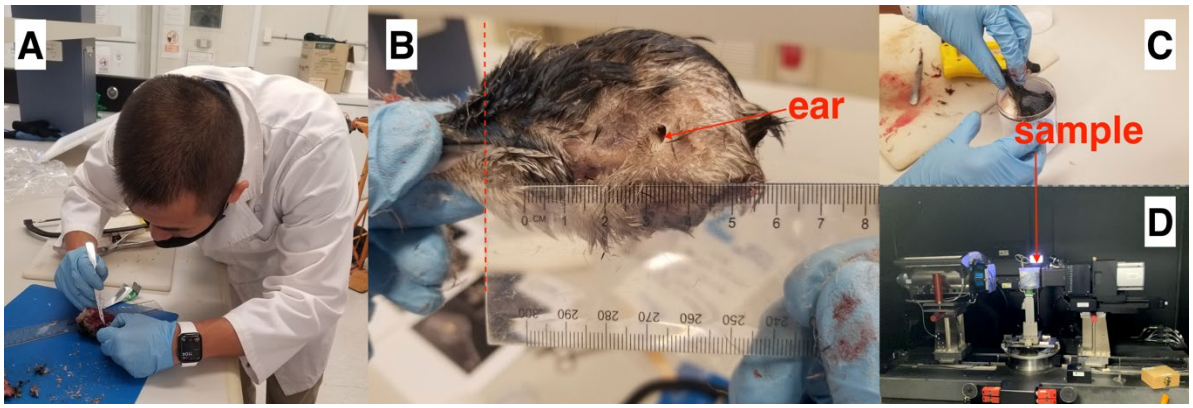

Figure 3. Dissection and microCT scanning of a penguin's head. (A) Dissection. (B) Preparation for microCT scanning. The red dashed line shows the position where the beak was removed. (C) Placing the sample into a plastic container. (D) MicroCT scanning.

The microCT data of the penguin's head included 1011 slices. The size of the ear structures of the little penguin is very small, for example, the length of the inner ear is ~14 mm and the length of the columella is ~5 mm. To assure the accuracy of the model reconstruction, we had to manually perform the segmentations slice by slice based on the penguin's anatomy to reconstruct the ear structures. The detailed ear structure 3D reconstruction is shown in Figure 4E. Figure 4 shows that the ear structure is located in the lower back of the skull. The ear structure contains mainly three parts: ear canal (in yellow), middle ear (in blue), and inner ear (in red) (Sadé et al., 2008; Frahnert et al., 2019). Like other birds, little penguins do not have external ear flaps. A pair of outer ear openings (round/oval holes) are located behind the eyes (Figure 3B) and covered by feathers. The other end of the ear canal is connected to the tympanic membrane (eardrum). The role of the tympanic membrane is to convey the received acoustic signals to the middle ear. The bony columella, the only auditory ossicle of the bird, is located inside the middle ear (the purple region in Figure 4E). The columella receives and transmits sounds from the tympanic membrane to the oval window through the columella's footplate, causing the perilymph of the inner ear to vibrate. The inner ear converts sounds to electronic signals for the nerve cells (Frahnert et al., 2019). Figure 4 displays the data analysis of the microCT data and 3D reconstruction of the head including the ear structures. All the geometries of the head structures were exported as a stereolithography (STL) file after optimization and modification of the raw data (i.e., smoothing, removing overlapping and self-intersections, etc.).

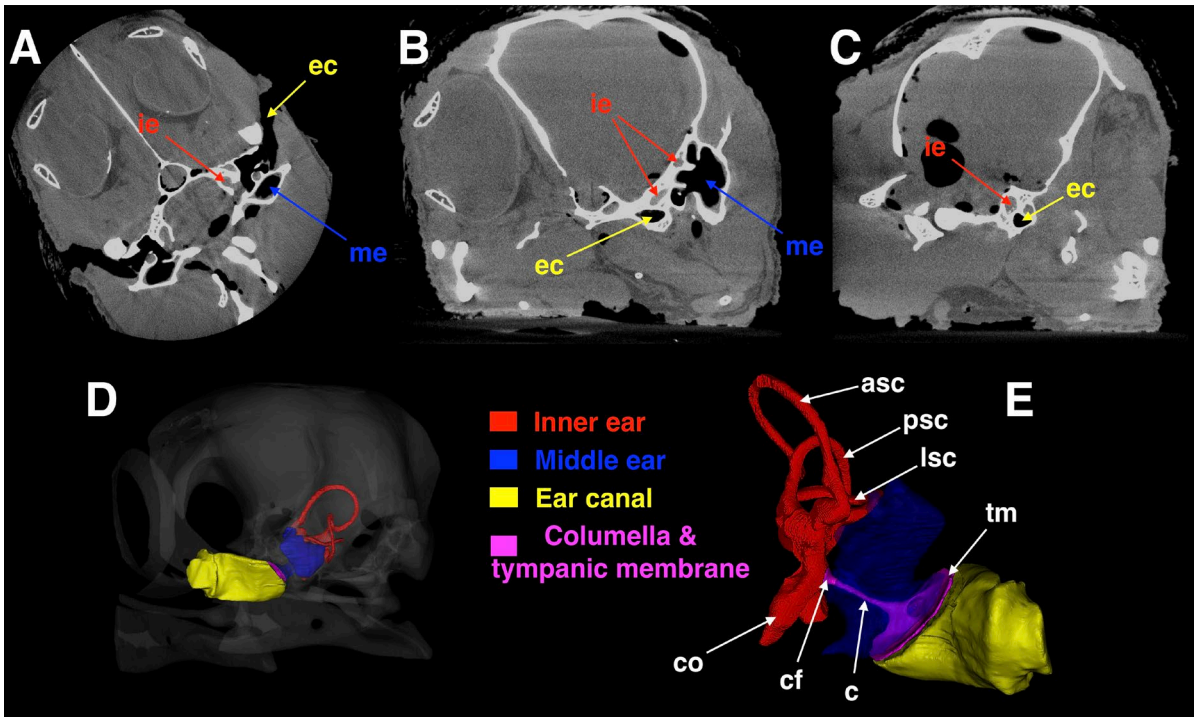

Figure 4. MicroCT scan data and the detailed 3D reconstruction of the ear. (A) Cross plane, (B) frontal plane, and (C) sagittal plane of the head. The grey level represents the different HU values. (D and E) 3D reconstruction of the skull and ear structures. The red region represents the inner ear, the blue region the middle ear, the yellow region the ear canal, and the purple region the columella and tympanic membrane. More details can be found in the supplementary files. Abbreviations used in figures: ie, inner ear; me, middle ear; ec, ear canal; co, cochlea; cf, columella's footplate; c, columella; tm, tympanic membrane; asc, anterior semicircular canal; psc, posterior semicircular canal; lsc, lateral semicircular canal.

3.4 Finite-Element Model Development

We developed detailed, anatomically accurate sound reception FE models based on high-resolution imaging data. The imaging-based FE modelling techniques allowed us to predict audiograms and study sound reception mechanisms in little penguins. Finite-element analysis (FEA) is a numerical technique for finding approximate solutions to boundary-value problems for partial differential equations. The advantage of FEA is the ability to deal with complex boundaries and to provide fine spatial information on the animal heads. The techniques have been used to study sound reception and hearing in several marine species, such as fish (Salas et al., 2019a, 2019b; Krysl et al., 2012; Wei et al., 2022), baleen whales (Cranford and Krysl, 2015; Tubelli et al., 2012; 2018), and toothed whales (Aroyan, 2001).

The STL files were imported into the COMSOL Multiphysics modelling software (Stockholm, Sweden) for FEA and corresponding data analysis. In this research, we studied both in-air (IA) and underwater (UW) hearing. We first built two FE hearing models based on the XCT data (sound reception in air and under water: the XCT-IA model and the XCT-UW model, respectively). While we were developing the XCT models, we found out that the XCT models could not be used to reconstruct the ear structure in detail. The slice thickness of the XCT was 1 mm, and the width of the inner ear was ~6 mm, which meant that less than 6 slices were available to reconstruct the inner ear. However, the slice thickness of the microCT data was 0.05 mm, resulting about 120 slices to be used for an inner ear reconstruction. Hence, we decided to build another two FE hearing models based on the microCT data (microCT-IA model and microCT-UW model). The setups of these models are shown in Figure 5.

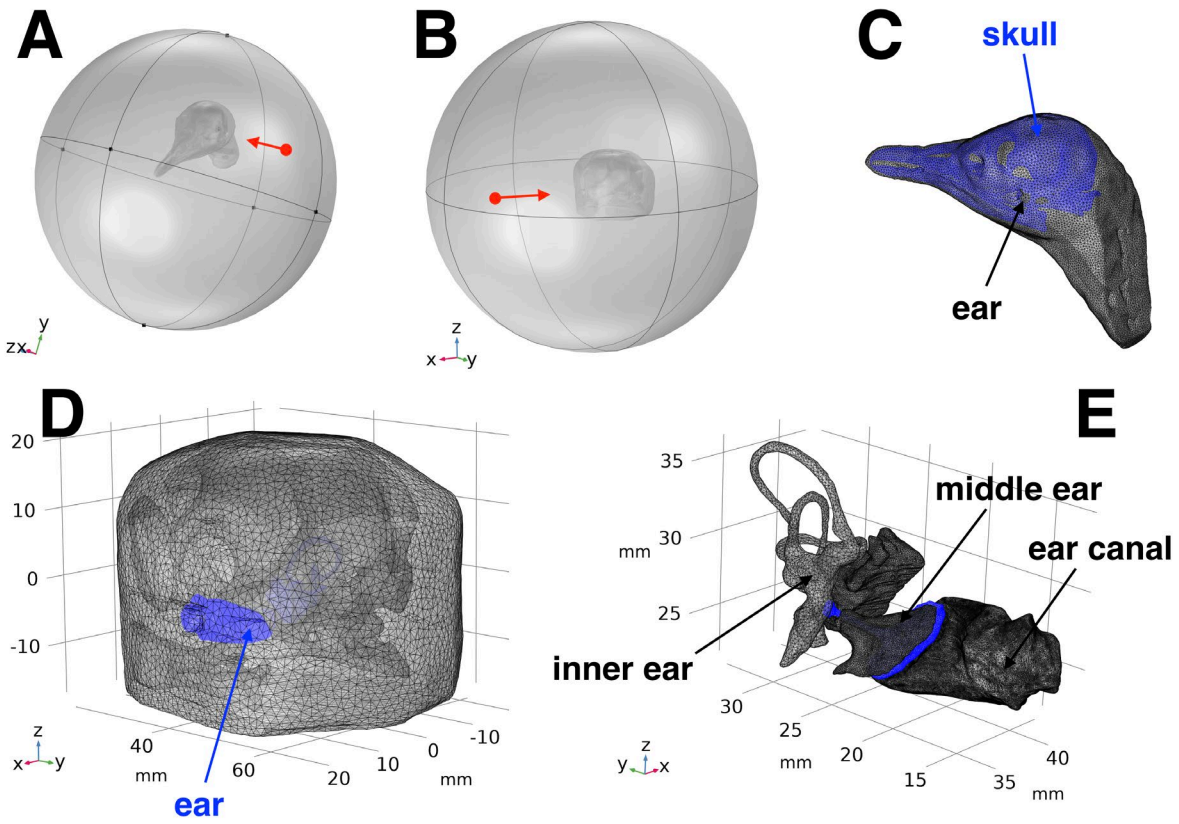

Figure 5. Little penguin FE hearing models. (A) The setup of the model based on XCT data. (B) The setup of the model based on microCT data. The red points represent the acoustic stimulus and the red arrows show the directions of the incoming sound (parallel to the x axis). (C) The meshing of the full head for the XCT model, the blue region represents the skull structure. (D) The meshing of the head for the microCT model, the blue region represents the ear structures. (E) The meshing of the ear structures, including the inner ear, middle ear, and ear canal.

All the models simulated the sound reception process from an outside media (air or seawater) to the inner ear of a little penguin. An air sphere and water sphere were set outside of the head for the IA and UW models, respectively, simulating a little penguin receiving sound through air and seawater, as shown in Figures 5A and B. The diameter of the sphere was set as 240 mm for the XCT models and 200 mm for the microCT models, respectively. A low-reflecting boundary condition (Bérenger, 1994) was applied to both spheres. The low-reflecting boundary condition is mainly intended for letting waves pass out from the model domain without reflection. In the real-life situation, penguins hear the sounds in a large domain. After the sounds travel through the penguin, they attenuate in the water with distance (very limited reflection). This low-reflecting boundary condition simulates the sound transmitting into free space with minimum boundary reflections. It also reduces the computational domain to a practical size while ensuring accurate simulation results.

To avoid any impact of the missing beak in the microCT models, as well as to make the XCT and the microCT models comparable, an incident acoustic wave was set in front of the left ear hole (60 mm from the ear hole on the left side of the head) with a given pressure amplitude for all models. The magnitude of the input pressure was arbitrary since the model was linear. The stimulus was directed towards the left side of the penguin's head at the selected frequencies, as the red arrows show in Figures 5A and B. The frequency was swept from 100 Hz to 10 kHz in steps of 200 Hz for both the IA and the UW models. The sound wave travelled through the air or sea water surrounding the head of

the penguin and then interacted with the complex head structures to generate traction loads on the surface of the ears.

The COMSOL's free mesher was used to generate a free tetrahedral mesh to map the entire model. The free mesh has a built-in detection for small features and narrow regions in a geometry. It also features an automatic element size adjustment for small features, narrow regions, and curved boundaries. It is widely accepted that the element size in element-based acoustic computations should be related to the wavelength. Often, the element size is measured in a certain (fixed) number of elements per wavelength. For the 3D acoustic modelling, the rule of thumb for meshing wave problems is to apply at least 5–6 second-order mesh elements per local wavelength in order to resolve waves, including resolving elastic waves in the solid (Thompson and Pinsky, 1994; Ihlenburg, 2006). In this study, the maximum mesh size was set to at least one-sixth of the wavelength at each frequency for each material (i.e., air, water, soft tissue, skull, etc.). To gain confidence in the accuracy of the model, a mesh refinement analysis/mesh convergence study conducted, testing progressively finer meshes to find the optimal element size for the model. Based on the mesh refinement results, the size of the element for air was set between 1 and 5 mm, for seawater between 1 and 15 mm, for soft tissues between 1 and 15 mm, for bony structures between 5 and 30 mm, and for ear structures (i.e., ear canal, inner ear, columella, etc.) between 1 and 5 mm. The XCT and microCT models used the same mesh setting. The meshing is shown in Figures 5 C, D, and E. The XCT and microCT models used the same mesh setting. The meshing is shown in Figures 5 C, D, and E. For the IA models, XCT-IA and microCT-IA , the geometry translated to a mesh consisting of 1.43 million and 1.79 million tetrahedral elements, with 2.31 million and 2.94 million degrees of freedom solved, respectively. For the UW models, XCT-UW and microCT-UW, the geometry translated to a mesh consisting of 1.43 million and 1.37 million tetrahedral elements, with 2.31 million and 2.38 million degrees of freedom solved, respectively. The mesh quality is shown in Figure 6.

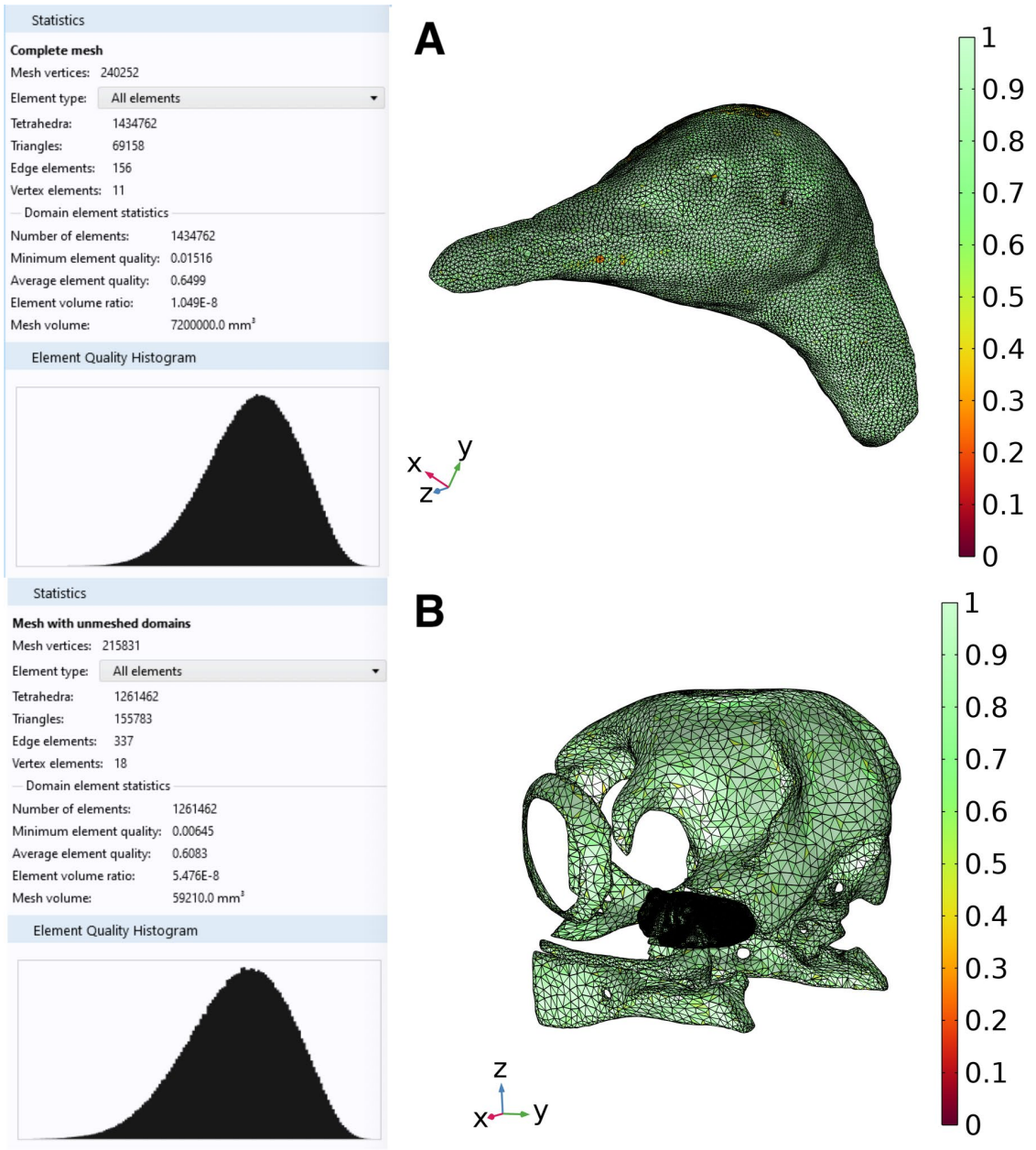

Figure 6. The mesh quality of the two models. (A) The mesh quality of the XCT model. (B) The mesh quality of the microCT model (the soft tissues were not shown in this figure). Note the different scales on the skull and ear canal. The colour scale shows the quality of the mesh elements, from red (poor) to green (good). The mesh element quality is a dimensionless quantity between 0 and 1, where 1 represents a perfectly regular element, in the chosen quality measure, and 0 represents a degenerated element.

The FE Pressure Acoustics-Frequency Domain module coupled with Solid Mechanics and an Acoustic-Structure Boundary was applied to the models. When acoustic waves propagate within a liquid medium, the longitudinal waves can be written as:

$$\frac{1}{\rho_0 c_s^2}\frac{\partial^2 p}{\partial t^2} + \nabla \cdot \left(-\frac{1}{\rho_0}\nabla p\right) = 0 \quad (1)$$

where p is the sound pressure (Pa), ρ_0 is the density (kg/m^3), and c_s is the speed of sound (m/s). The density ρ_0 is included in the equation because of its variations in different computational domains

within the model. For the harmonic solution of the pressure $p(\boldsymbol{x},t) = p(\boldsymbol{x})e^{i\omega t}$, with the angular frequency ω (rad/s), Eq. 1 can be simplified as:

$$\nabla \cdot \left(-\frac{1}{\rho_0}\nabla p\right) - \frac{\omega^2 p}{\rho_0 c_s^2} = 0 \quad (2)$$

While the acoustic waves interact with the solid medium, the multiphysics coupling provides and assigns the boundary conditions for the two-way acoustic structural coupling between the liquid (e.g., water and soft tissues) and the solid (e.g., skull and columella). The fluid-solid boundary condition includes the following interaction between fluid and solid domains:

$$\boldsymbol{F} = -\boldsymbol{n}_s p \quad (3)$$

$$-\boldsymbol{n}_a \cdot (-\frac{1}{\rho_0}\nabla p) = a_n \quad (4)$$

$$a_n = (\boldsymbol{n}_a \cdot \boldsymbol{u})\omega^2 \quad (5)$$

where $\boldsymbol{F}$ is the boundary load (force/unit area) on solid, $\boldsymbol{n}_s$ is the outward-pointing unit normal vector seen from inside the solid, p is the acoustic pressure, $\boldsymbol{n}_a$ is the outward-pointing unit normal vector seen from inside the liquid, ρ_0 is the density, a_n is normal acceleration of the solid surface in the liquid domain boundary, and $\boldsymbol{u}$ is the calculated harmonic displacement vector of the solid structure.

3.5 Reconstruction of Material Properties

None of the material properties have been experimentally measured for little penguins but referring to existing literature and knowledge of anatomical similarities (Buhler, 1992; Dumont, 2010; Azhari, 2010), physiologically relevant values for the properties can be estimated. For simplicity, all the bony structures (e.g., skull) and soft tissue components (e.g., muscles) in the XCT and microCT models were modelled as homogeneous, isotropic, and linear. There were no measured values available for Young's modulus (the ratio of stress to strain that describes the stiffness of materials) and Poisson's ratio (a ratio of transverse strain to longitudinal strain for bone) for the bones and the columella of the little penguin, therefore, the common values for solid bone structures in vertebrates were used in this study (Tubelli et al., 2014). The detailed values of material properties applied in the models are shown in Table 1.

Table 1. Material property values for the little penguin hearing models.

Material	Sound Speed (m/s)	Density (kg/m^3)	Young's modulus (MPa)	Poisson's ratio
Sea water	1500	998		
Bony structures	3500	2.3´10^3	60´10^3	0.3
Soft tissues	1500	1100		
Inner ear	986	1466		
Columella	3500	2.3´10^3	35´10^3	0.3

3.6 Transfer Function

The ear (i.e., external, middle, and inner ear) can be seen as a series of components. The synergistic response of these ear components to incoming acoustic signals can together be used to determine the audiogram (Tubelli et al., 2012; 2018; Cranford and Krysl, 2015). When the incident acoustic wave impinges upon the animal's head, it partially reflects off the skin and feathers and partially propagates further into the soft tissues (e.g., muscle). Some of the waves travel through the dense bony structures as elastic waves. The ears vibrate under the incident acoustic wave (p_{input}), resulting in the motion of the columella within the oval window, which produces a velocity at the columella's footplate (v_{cf}). The motion of the columella's footplate pushing in and out of the oval window drives the cochlea mechanically, causing the perilymph in the inner ear to vibrate. Based on this sound reception mechanism, the output of the model is a frequency-dependent transfer function between the magnitude of the velocity at the columella's footplate (v_{cf}) and amplitude of the input sound pressure (p_{input}), giving a transfer function with the units of (nm/s)/Pa. This columella velocity transfer function

(CVTF, p_{input} to v_{cf}) was only calculated for microCT models (microCT-IA and microCT-UW models). The XCT data have a relatively low resolution, thus, the tiny columella reconstruction for the XCT models was not as detailed as the one for the microCT models. Therefore, the velocities at the columella's footplate in the XCT models were difficult to calculate. Instead, we calculated the pressure transfer function (PTF) for the XCT models to study the transformation of incident pressure at the cochlea when the sound pressure waves travel through the outer media and various internal animal soft tissues in the sound reception process. The relative amplitude of the received pressure at the cochlea (p_{co}) versus the incident pressure (p_{input}) is the representation of the PTF.

3.7 Audiogram Curve

The audiogram was predicted based on the transfer function. The audiogram curve was calibrated with respect to the minimum audible pressure. For example, Cranford and Krysl (2015) assumed the hearing threshold of the fin whale to be similar to that measured for bottlenose dolphins and killer whales (~70 dB re 1µPa). Based on this, the minimum threshold pressure across all frequencies was estimated. Unfortunately, audiograms have not been measured for little penguins (or any other penguin species), neither in air nor under water; only the sensitivity range of backfooted penguins (in-air) was measured by Wever et al. (1969) using the cochlear potential method. Therefore, this study referred to the values of the stapes velocity calculated at the threshold for other terrestrial species from the literature to convert the transfer function (Tubelli et al., 2012).

4 Results

Our FE models simulated the sound reception process of a little penguin's head in air and under water. The sound pressure fields at each of the excitation frequencies were calculated. Figure 7 shows an example of the sound pressure field at 1000 Hz exported from the XCT-UW model. The incident acoustic stimulus travelled through the water, directly toward the head of a little penguin from the left side. The figure shows that relative the sound pressure at the left ear was significantly higher than that at the right ear because the left ear was closer to the sound source excitation.

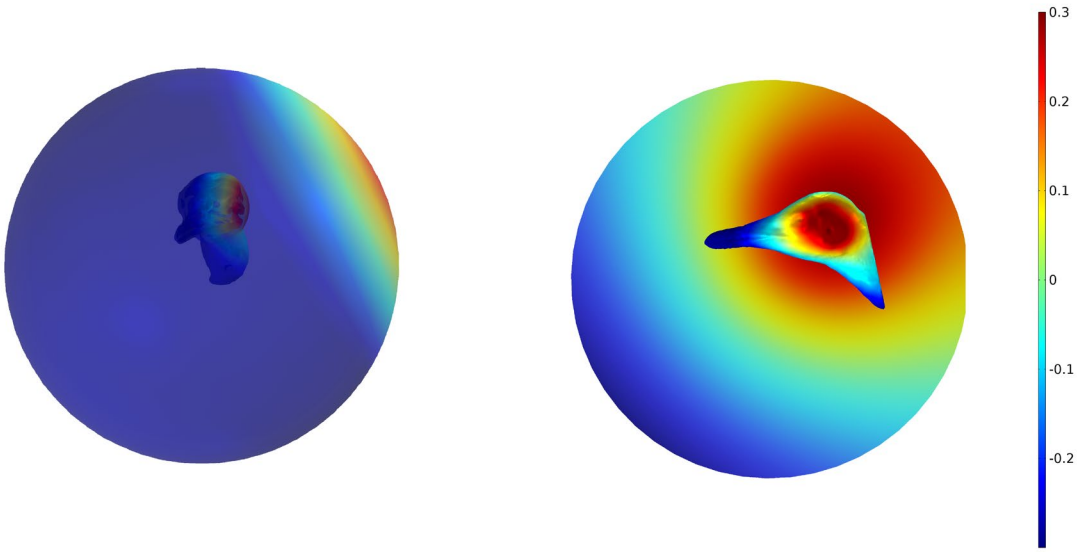

Figure 7. Sound pressure field of XCT model at 1000 Hz. The colour scale shows the relative amplitude of the sound pressure, which was normalized by dividing by the maximum values in the results (more details about sound reception can be found in the supplementary files).

After the acoustic stimulus interacted with the complex head structures (i.e., soft tissues, ear apparatus, skull, etc.), the elastic waves generated motion within the stiff and dense skull causing the skull deformation (more details about skull deformation can be found in the supplementary files). The skull vibration also created displacement of the skull. We calculated the displacement fields at each of the excitation frequencies. Figure 8 shows the examples of displacement fields of the XCT-UW model and the microCT-UW model at 2000 Hz.

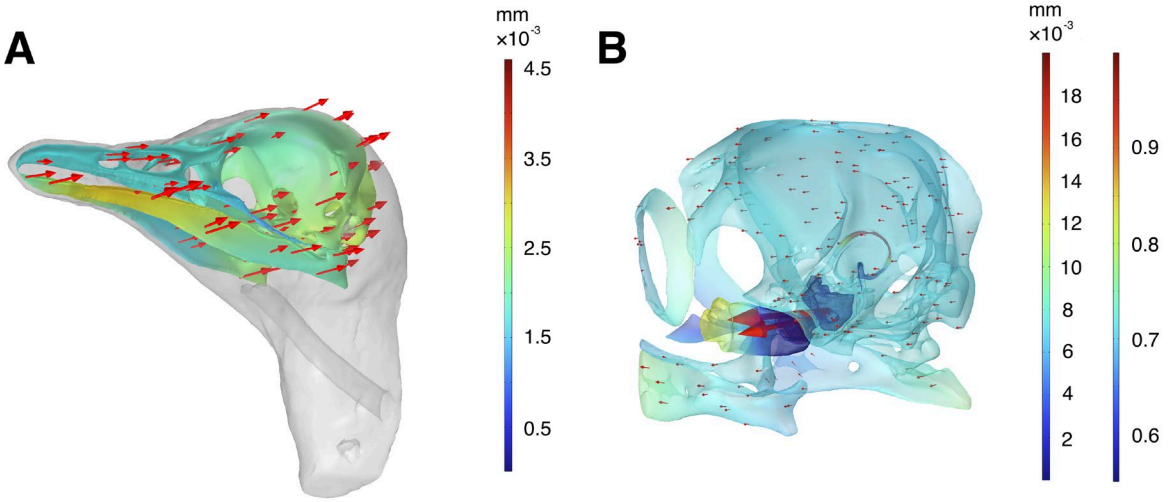

Figure 8. Two examples of the displacement fields of the XCT-UW and the microCT-UW models at 2000 Hz. The red arrows indicate both the direction and magnitude of the displacement. (A) The displacement field of the skull in the XCT-UW model, the grey region represents the soft tissues surrounding the skull. The colour bar indicates the relative magnitude of the displacement. (B) The displacement field of the skull and columella, as well as the sound pressure field of the ear apparatus in the microCT-UW model (soft tissues are not shown here). The colour bar indicates the relative magnitude of the displacement and the relative amplitude of sound pressure, respectively.

The direction of the displacement in both the XCT-UW and the microCT-UW models was towards the left side of the head. This was due to the left side source excitation generating a force acting on the particles to restore them to their original position. In Figure 8B, higher displacement regions were also visible inside the ear apparatus of the microCT-UW models. To understand the motion of the columella during sound reception better, we compared the columella's response to incident acoustic waves in the frequency range from 1 kHz to 10 kHz was compared, as shown in Figure 9.

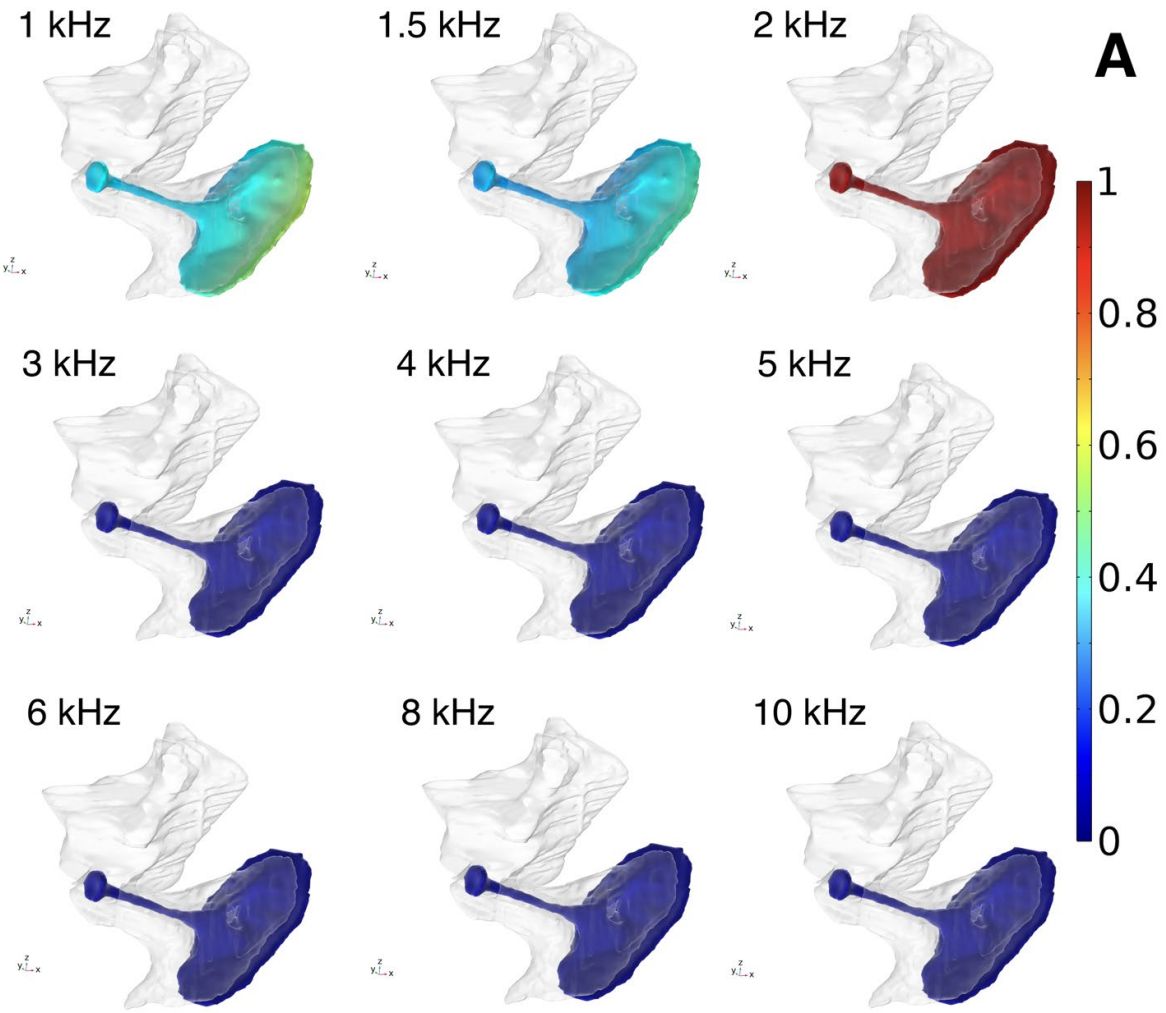
1 kHz
1.5 kHz
2 kHz
A
1
0.8
0.6
0.4
0.2
0
3 kHz
4 kHz
5 kHz
6 kHz
8 kHz
10 kHz

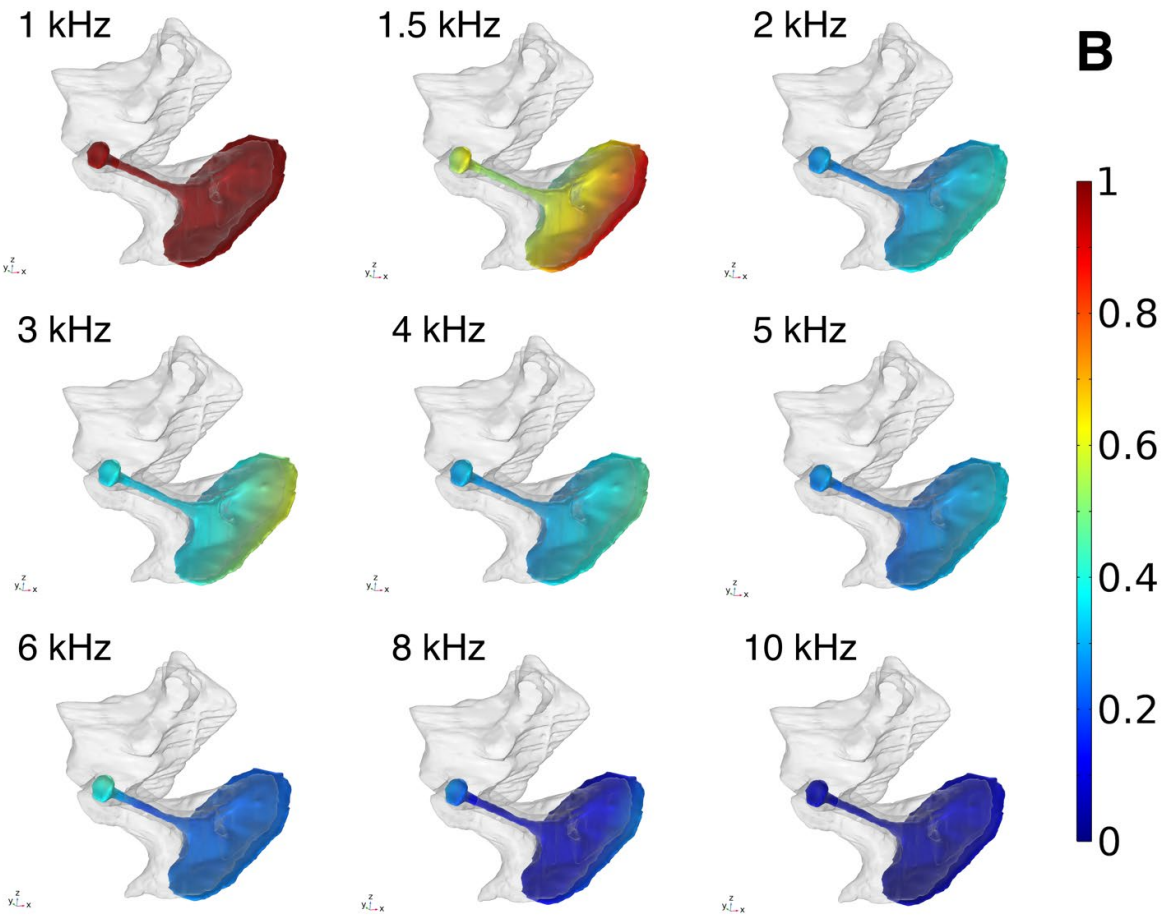

Figure 9. Motion of the columella for incident sounds from 1 kHz to 10kHz. The colour bar indicates the relative magnitude of the velocity. The transparent part represents the middle ear. (A) Columella motion of the microCT-IA model. (B) Columella motion of the microCT-UW model.

When the incident sound travels through the ear canal, it causes the tympanic membrane to vibrate. The bony columella acts as an elastic object to vibrate when it is driven by the incident stimulus, creating velocity and displacement. The motion in the columella causes the motion at the columella's footplate, which sits in the oval window of the cochlea. To better examine the motion of the columella during sound reception, the columella in response to the incident acoustic waves in the frequency range from 1 kHz to 10 kHz was compared in both microCT models, as shown in Figure 9. The results showed that the best frequency response range of the columella to the incoming sound was around 1−2 kHz for the microCT-IA model and 1−1.5 kHz for the microCT-UW model. In the microCT-IA model, with frequencies higher than 2 kHz, the motion of the columella was significantly reduced and became stationary. In the microCT-UW model, the motion was also reduced when the frequency was above 2 kHz. The columella became relatively stationary when the frequency was higher than 8 kHz.

Early work indicated that the audiogram is shaped by the external, middle, and inner ear connected in series, with the external and middle ear acting as the main contributors to low and mid frequencies for the audiogram (Ruggero and Temchin, 2002). Little penguins do not have external ear flaps, therefore constructing an accurate ear model with the ear canal, middle ear, and inner ear is critical for predicting their audiograms. In the first couple of months, our work focused on building models based on XCT scan data. Although we examined multiple XCT data based on different individuals/scan settings/reconstruction methods, the columella and part of the inner ear (semicircular canals) were too small to be reconstructed in detail due to the relatively lower resolution of the XCT data. The XCT

data can be used to construct the ear canal, middle ear, cochlea, and other larger head structures, such as the skull and soft tissues. Therefore, as we mentioned in the previous section (3.4), we only calculated the PTF for both the XCT-IA and the XCT-UW models, a transfer function between the amplitude of the incident sound pressure wave and the amplitude of input sound pressure at the cochlea. Considering the microCT models were accurately built based on the high-resolution microCT data, especially the ear canal, middle ear, columella, and inner ear were constructed in detail. Furthermore, CVTF is a transfer function between the amplitude of the incident sound pressure wave and the magnitude of the velocity of the columella's footplate. Using CVTF to predict the audiogram is a reliable method since it considers both the motion of the solid materials and the sound pressure on the fluid materials in the animal's head (Cranford and Krysl, 2015). Therefore, we calculated the CVTF for the microCT models. The comparisons between the PTFs of the XCT models and CVTFs of the microCT models are shown in Figure 10.

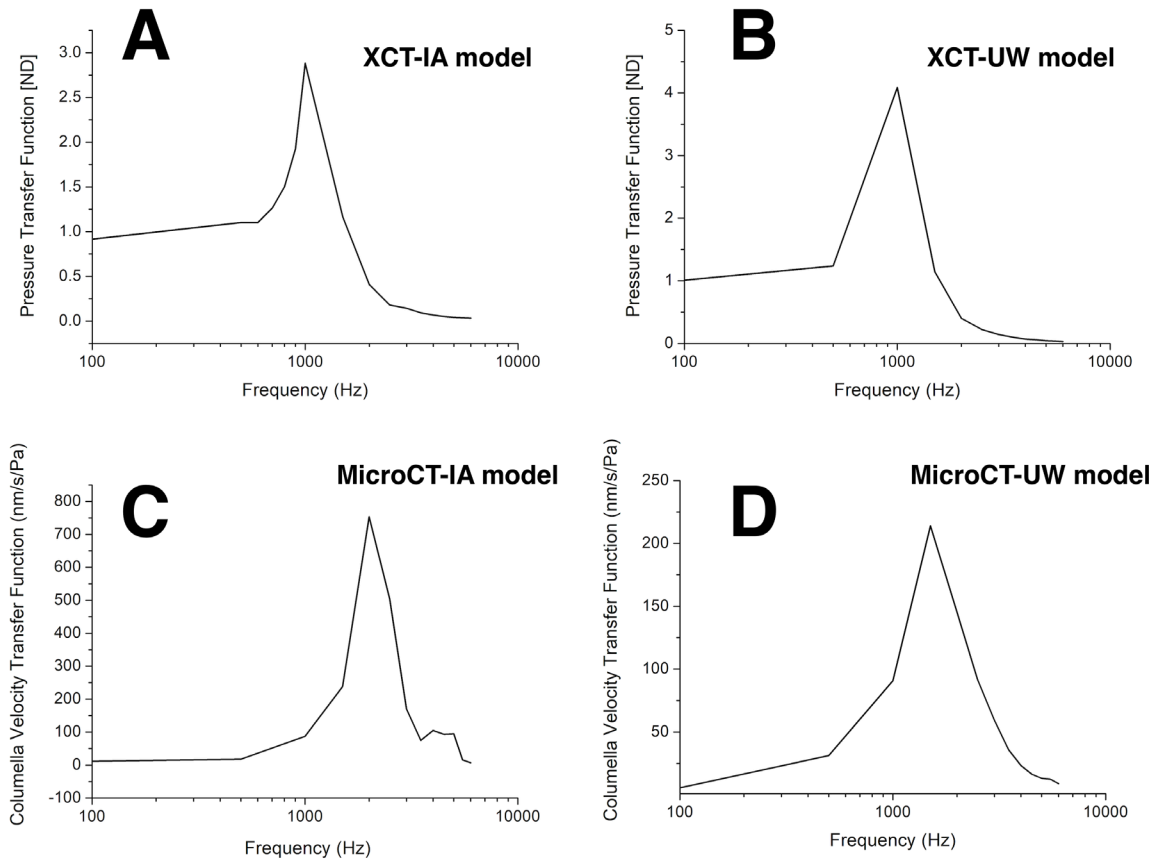

Figure 10. Pressure transfer function (PTF) and columella velocity transfer function (CVTF) for the XCT and the microCT models. (A) PTF of the XCT-IA model. (B) PTF of the XCT-UW model. (C) CVTF of the microCT-IA model. (D) CVTF of the microCT-UW model.

Figure 10 shows that the peak response frequencies of the XCT models (XCT-IA and XCT-UW models) were both around 1000 Hz, whereas the peak response frequencies of the microCT-IA model and the microCT-UW model were approximately 2000 Hz and 1800 Hz, respectively. All the TFs attenuated sharply at higher frequencies. Although the peak response frequencies of the XCT models were lower than those of the microCT models, the values were similar to the hearing range of other diving birds (Mooney et al., 2019a; 2019b; 2020; Smith et al., 2023a, 2023b, 2023c). Early tape recordings have shown that the "grunt" and "bray" sounds made by black-footed penguins had the most prominent frequencies below 2000 Hz (e.g., some of the "brays" mainly contained frequencies between 1200 Hz and 1700 Hz) (Wever, et al., 1969). Therefore, our results were consistent with vocalizations of black-

footed penguins. Finally, we decided to use the CVTFs of the microCT models to predict the audiograms for the little penguin as shown in Figures 11 and 12.

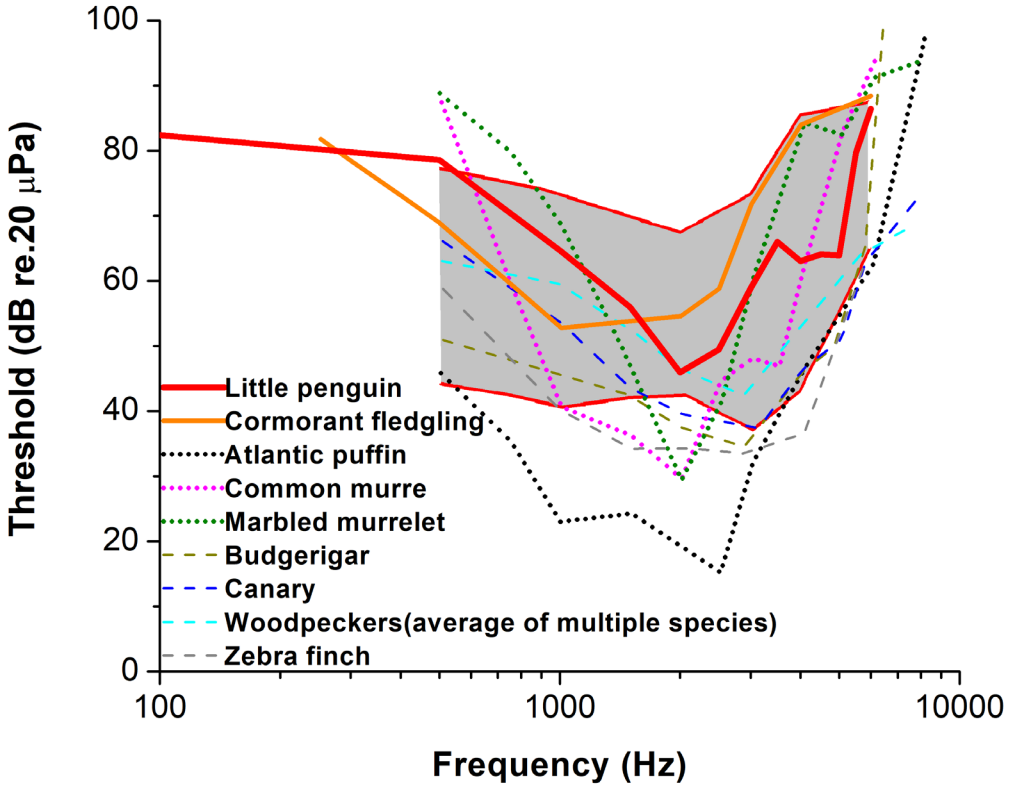

Figure 11. Predicted in-air audiogram of the little penguin (red solid line) and in-air audiograms from measured aerial hearing thresholds of other birds. The dotted lines denote the audiograms of several alcid diving birds, including Atlantic puffin *Fratercula arctica* (Mooney et al., 2020), common murre *Uria aalge* (Smith et al., 2023a), and marbled murrelet *Brachyramphus marmoratus* (Smith et al., 2023b). The dashed lines denote the audiograms of several terrestrial birds, including budgerigar *Melopsittacus undulatus* (Brittan-Powell et al., 2002), canary *Serinus canaria* (Brittan-Powell et al., 2010), woodpeckers (average of multiple species, Lohr et al., 2013), and zebra finch *Taeniopygia guttata* (DeAngelo, 2008). The solid lines denote non-alcid diving birds, including little penguin (this study) and cormorant fledgling *Phalacrocorax carbo sinensis* (Larsen et al., 2020). The grey region shows the mean auditory evoked potential (AEP) aerial hearing range of other non-alcid diving bird species from Crowell et al. (2015).

For the in-air audiogram, the lowest predicted in-air threshold (~46 dB re 20 µPa) for the little penguin was found at ~2 kHz with a gradual increase in thresholds at lower frequencies and a steeper increase at higher frequencies (>5 kHz). The region of best sensitivity (based on the lowest 30 dB range) was found at ~550 Hz–5400 Hz.

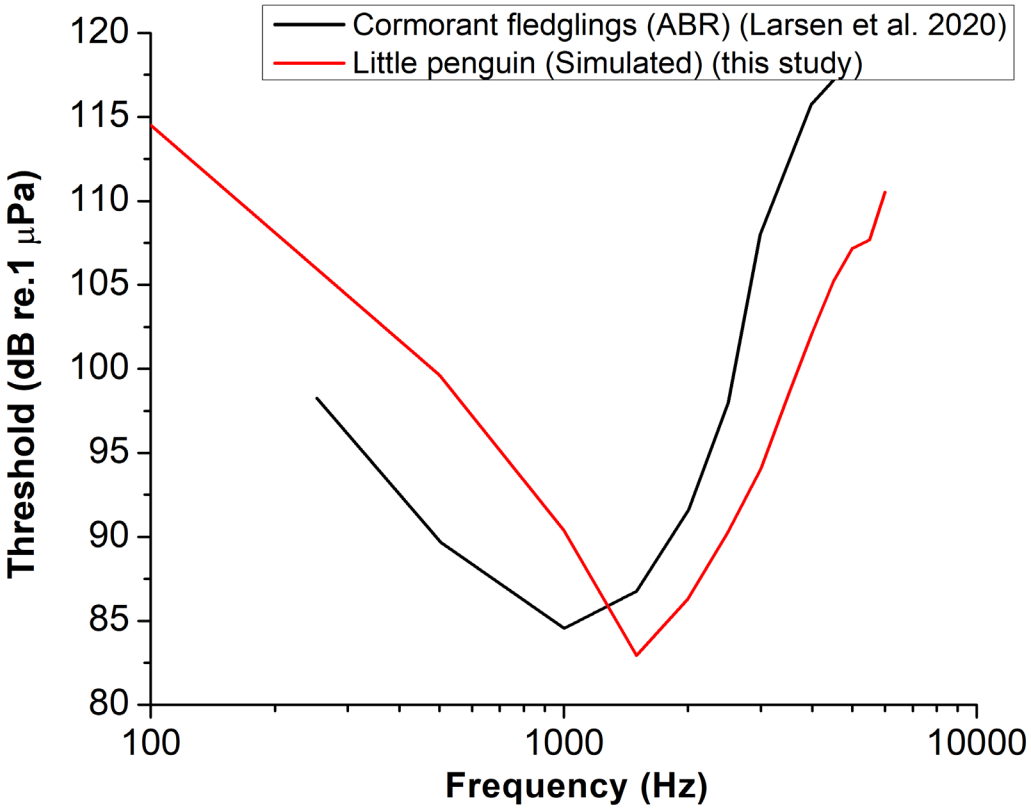

Figure 12. Predicted underwater audiogram of the little penguin. The underwater audiogram was compared to the data measured for the cormorant fledglings by Larsen et al. (2020).

For the underwater audiogram, the lowest predicted underwater threshold was at ~83 dB re 1 µPa at ~1.5 kHz. The region of best sensitivity was found at ~200 Hz – 6000 Hz. Above this range, the hearing sensitivity fell off precipitously.

5 Discussion

5.1 Predicted Audiograms

In general, our predicted audiograms were comparable with those of other diving birds in both the form and range of auditory sensitivity.

Wever et al. (1969) used cochlear potential methods to study aerial hearing in black-footed penguins (also a small penguin species). Based on the results from three black-footed penguins, the best auditory acuity was found from 600 Hz to 5000 Hz. Therefore, our predicted in-air audiogram (Figure 11) closely aligned with the data obtained from the black-footed penguins. Furthermore, the shape of our in-air audiogram curve (Figure 11) was similar to those of aerial audiograms of other bird species, including both diving and terrestrial birds, albeit the lowest threshold of little penguins was higher than those of the three alcid diving birds, Atlantic puffin (Mooney et al., 2020), common murre (Smith et al., 2023a), and marbled murrelet (Smith et al., 2023b). Penguins are *Spheniscids* (non-alcid diving birds). Our predicted in-air audiogram curve was closer to those of other non-alcid diving birds. Our audiogram curve fell well into the mean AEP audiograms of several non-alcid diving bird species from the previous

study (Crowell et al., 2015) and is also comparable to the aerial auditory brainstem response (ABR) audiogram of the cormorant fledgling (Larsen et al., 2020).

Very little is known about underwater audiograms of diving birds; only one study by Larsen et al. (2020) has measured the underwater ABR audiogram for cormorant fledglings (the red curve in Figure 12). Our predicted underwater audiogram showed a similar frequency-dependent pattern of sensitivity to the data from Larsen et al. (2020), with a slightly lower sensitivity (~2 dB) and a slightly higher sensitive frequency range (~500 Hz).

Furthermore, Larsen et al. (2020) was the only study that provided a robust comparison of in-air and underwater hearing thresholds in a diving bird (great cormorant). Their results indicate that mean hearing thresholds across individuals were similar between the two environments, suggesting that diving birds might share a similar trend in terms of in-air and underwater audiograms (Smith et al., 2023a; 2023b). In our study, the two predicted audiograms of little penguins (Figures 11 and 12) also showed a similar trend, supporting the assumption by Larsen et al. (2020).

Our predicted in-air audiogram is relatively less sensitive compared to those of most diving birds depicted in Figure 11. We used the stapes velocity calculated at the threshold for other terrestrial species from the literature for the interpretation of the CVTF (Tubelli et al., 2012). We ran some tests by using different values of stapes velocity from multiple terrestrial species to convert the CVTF; the outcomes shifted ~±5 dB across the frequencies, which all fell well into the mean hearing range of non-alcid diving birds in air (the grey region in Figure 11, Crowell et al., 2015). Moreover, it should be noted that the slope of our in-air audiogram at the lower frequencies (below 500 Hz) was slightly different from the measured ones. It may be due to differences between species (e.g., anatomical differences) rather than a result of the missing beak in the microCT models since the transfer functions in XCT models (Figures 10A and B) have a similar trend at the lower frequencies. It should also be noted that the anatomical configuration of the individual varies with sex, age, health etc., causing slight differences when sound interacts with the animal structures. Thus, audiograms among individuals of the same species would also be slightly different. Therefore, modelling more little penguin specimens of different sex and age is important in future work to capture the variability in audiograms of this species.

Sørensen et al. (2020) documented the detection of underwater sound for Gentoo penguins. Their results found that Gentoo penguins had strong responses at 120 dB re 1 µPa when an acoustic stimulus with frequencies between 200 and 6000 Hz was played in a large water tank. Previous studies found that humans usually have strong behavioural responses when they hear sounds 50 dB above their hearing threshold (Sørensen et al., 2020). For marine mammals, strong behavioural reactions were observed when the received levels were greater than 100 dB above the hearing threshold (Southall et al., 2008). Our predicted underwater audiogram might be able to explain why Sørensen et al. (2020) did not record a reaction at 100 dB re 1µPa. Our predicted audiogram showed the lowest threshold was at ~83 dB re 1µPa, and thus the penguins should be able to hear 100 dB sounds. The 100 dB re 1µPa sounds might not be loud enough to elicit a reaction.

5.2 The Limitations of the Models and Future Work

Note that the audiograms we predicted in this study are only approximations. There were some limitations that need to be addressed and improved in future studies. Due to little penguins being very small (the length of an adult little penguin is only ~30 cm), it is difficult to collect large enough soft tissues for tissue property measurement. For example, measuring sound speed in the muscles using an ultrasonic velocimeter requires collecting multiple samples with a thickness of at least 1 cm, which is impossible for little penguins. There are also no relevant data available for any penguin species that could be used as proxy. Therefore, we had to input values for tissue properties based on existing literature and knowledge of anatomical similarities from other bird species (Buhler, 1992; Dumont, 2010; Azhari, 2010). The same methods were commonly used in previous FEA studies (Aroyan, 2001; Tubelli et al., 2012; 2018; Cranford and Krysl, 2015; Wei and McCauley, 2022). Therefore, the sensitivity

tests were performed by inputting different parameters for comparison. The sensitivity test results showed very little sensitivity when the input parameters were slightly changed.

Previous studies using FEA to estimate hearing thresholds of baleen whales have shown that different locations of source excitation could cause reasonably different response curves (Tubelli et al., 2012; 2018). Therefore, it would be important to test this theory on the little penguin models in future. This requires to first perform microCT scans on a full penguin head. In this study, the beak was removed to fulfil the size requirement for microCT scanning (~40 mm × 40 mm × 40 mm). To avoid the effect of the missing beak, we only located the source excitation in front of the left ear (Figure 5).

5.3 Potential Effects of Anthropogenic Noise on Little Penguins

The soundscape of many coastal areas is changing due to increased anthropogenic activity in these areas, resulting in seabirds, including little penguins facing progressive acoustic habitat degradation. The modelling results here indicate that hearing frequencies of little penguins overlap with many anthropogenic noise sources, both in air and under water. For example, the noise sources in air, such as traffic noise, human speech, offshore constructions, and passing aircraft are audible to little penguins (see Schoeman et al. 2022 for an overview of in-air noise spectra). Under water, ship traffic is a primary source of noise between 20 and 1000 Hz (Urick, 1983). Pile driving is common in coastal regions undergoing development, emitting broadband acoustic energy between 50 Hz and 5 kHz (e.g., Erbe, 2009). Another noise source in the ocean are airgun signals from seismic surveys, with most acoustic energy below 500 Hz (e.g., Erbe and King, 2009). Military sonar typically ranges between 1 and 10 kHz (Nowacek et al., 2007). It appears that these noises are detectable by little penguins, which may induce various behaviours. Our results indicate that this species is susceptible to disturbance from a range of anthropogenic noise types both in air and under water.

6 Conclusions/Recommendations

This is the first study that uses imaging-based FE modelling to predict auditory sensitivity in the little penguin both in air and under water. It is the only currently available method capable of predicting hearing sensitivities for sound reception in little penguins over a broad frequency range, between 100 Hz and 10 kHz. The results provide a valuable indication of the ranges of frequencies and thresholds that can be heard by little penguins. The predicted audiograms also show good agreement with other diving birds in both the form and range of auditory sensitivity. The study develops important tools to study the sound reception process and predict auditory sensitivity for inaccessible animals, if an animal species shares a similar sound reception mechanism. Finally, this study provides critical information for marine conservation efforts as the outputs from this study can inform noise impact mitigation and conservation management strategies.

7 References

Aroyan JL (2001) Three-dimensional modeling of hearing in *Delphinus delphis*. J Acoust Soc Am 110(6): 3305–3318.

Azhari H (2010) Appendix A: Typical scoustic properties of yissues. In: Basics of biomedical ultrasound for engineers. IEEE, pp. 313–314.

Bayne, EM, Bayne EM, Habib L, Boutin S (2008) Impacts of chronic anthropogenic noise from energy-sector activity on abundance of songbirds in the boreal forest. Conserv Biol 22: 1186–1193.

Bérenger JP (1994) A perfectly matched layer for the absorption of electromagnetic waves. J Comput Phys 114(2): 185–200.

Brittan-Powell EF, Dooling RJ, Gleich O (2002) Auditory brainstem responses in adult budgerigars (*Melopsittacus undulatus*). J Acoust Soc Am 112: 999−1008.

Brittan-Powell EF, Dooling RJ, Ryals B, Gleich O (2010) Electrophysiological and morphological development of the inner ear in Belgian Waterslager canaries. Hear Res 269: 56−69.
Buhler P (1992) Light bones in birds. LA Mus Nat Hist Sci Ser 36: 385–394.
Cannell BL, Kendall WL, Tyne JA, Bunce M, Hetzel Y, Murray D, Radford B (2023) Marine heatwaves affect breeding, diet and population size but not body condition of a range-edge little penguin colony. Mar Ecol Prog Ser: HEATav11.
Clark CW (1990) Acoustic behavior of mysticete whales. In: Thomas JA, Kastelein RA (eds), Sensory abilities of cetaceans: Laboratory and field evidence. New York: Plenum Publishing Corporation. pp. 571–583.
Cranford TW, Krysl P (2015) Fin whale sound reception mechanisms: Skull vibration enables low-frequency hearing. PLoS ONE 10(1): Article e0116222.
Crowell SE, Wells-Berlin AM, Carr CE, Olsen GH, Therrien RE, Yannuzzi SE, Ketten DR (2015) A comparison of auditory brainstem responses across diving bird species. J Comp Physiol A Neuroethol Sens Neural Behav Physiol 201: 803−815.
DeAngelo KM (2008) Assessing hearing loss due to ototoxic drugs in the zebra finch. Master dissertation, University of Maryland, College Park.
De Greef D, Pires F, Dirckx JJ (2017) Effects of model definitions and parameter values in finite element modeling of human middle ear mechanics. Hear Res 344: 195–206.
Dumont ER (2010) Bone density and the lightweight skeletons of birds. Proc R Soc B 2772193–2198.
Erbe C (2009) Underwater noise from pile driving in Moreton Bay, Qld. Acoust Aust 37 (3): 87–92.
Erbe C, Duncan A, Vigness-Raposa KJ (2022) Introduction to sound propagation under water. In: Erbe C, Thomas JA (eds) Exploring animal behavior through sound: Volume 1: Methods. Springer International Publishing, Cham, pp. 185–216.
Erbe C, King AR (2009) Modelling cumulative sound exposure around marine seismic surveys. J Acoust Soc Am 125 (4): 2443–2451.
Erbe C, Marley S, Schoeman R, Smith JN, Trigg L, Embling CB (2019) The effects of ship noise on marine mammals--A review. Front Mar Sci 6: 606.
Frahnert S, Lindner M, Bendel E, Frahnert, KH, Westphal, N, Dahne M (2019) 3D-visualization of the ear morphology of penguins (*Spheniscidae*): Implications for hearing abilities in air and underwater. Proc Mtgs Acoust 37: 010018.
Francis CD, Kleist NJ, Davidson BJ, Ortega CP, Cruz A (2012) Behavioral responses by two songbirds to natural-gas-well compressor noise. Ornithol Monogr 74(1): 36–46.
Gan RZ, Feng B, Sun Q (2004) Three-dimensional finite element modeling of human ear for sound transmission. Ann Biomed Eng 32(6): 847–859.
Goerlitz HR, Greif S, Siemers BM (2008) Cues for acoustic detection of prey: insect rustling sounds and the influence of walking substrate. J Exp Biol 211: 2799–2806.
Homma K, Du Y, Shimizu Y, Puria S (2009) Ossicular resonance modes of the human middle ear for bone and air conduction. J Acoust Soc Am 125(2): 968–979.
Homma K, Shimizu Y, Kim N, Du Y, Puria S (2010) Effects of ear-canal pressurization on middle-ear bone- and air-conduction responses. Hear Res 263(1): 204–215.
Ihlenburg F (2006) Finite element analysis of acoustic scattering (Springer Science, Business Media).
Ketten DR (1994) Functional analysis of whale ears: adaptations for underwater hearing. IEEE Proc Underwater Acoust 1: 264–270.
Ketten DR (1997) Structure and function in whale ears. Bioacoustics 8: 103–135.
Ketten DR (2000) Cetacean ears. In: Au WWL, Popper AN, Fay RR (eds), Hearing by whales and dolphins. New York: Springer-Verlag. pp. 43–108.
Koike T, Wada H, Kobayashi T (2002) Modeling of the human middle ear using the finite-element method. J Acoust Soc Am 111(3): 1306–1317.
Krysl P, Hawkins AD, Schilt C, Cranford TW (2012) Angular oscillation of solid scatterers in response to progressive planar acoustic waves: do fish otoliths rock? PLoS ONE 7: e42591.
Larsen ON, Wahlberg M, Christensen-Dalsgaard J (2020) Amphibious hearing in a diving bird, the great cormorant (*Phalacrocorax carbo sinensis*). J Exp Biol. 17: 223(6): jeb217265.

Lohr B, Brittan-Powell EF, Dooling RJ (2013) Auditory brainstem responses and auditory thresholds in woodpeckers. J Acoust Soc Am 133: 337−342.
Matthews JN, Rendall LE, Gordon JCD, Macdonald DW (1999) A review of frequency and time parameters of cetacean tonal calls. Bioacoustics 10: 47–71.
Mooney TA, Smith AB, Larsen ON, Hansen KA, Wahlberg M, Rasmussen MH (2019a) Field-based hearing measurements of two seabird species. J Exp Biol 222: jeb190710.
Mooney TA, Smith AB, Hansen KA, Larsen ON, Wahlberg M, Rasmussen MH (2019b) Birds of a feather: hearing and potential noise impacts in puffins (*Fratercula arctica*). Proc Mtgs Acoust 37: 010004.
Mooney TA, Smith AB, Larsen ON, Hansen KA, Rasmussen MH (2020) A field study of auditory sensitivity of the Atlantic puffin, *Fratercula arctica*. J Exp Biol 223: jeb228270.
Nowacek DP, Thorne LH, Johnston DW, Tyack PL (2007) Responses of cetaceans to anthropogenic noise. Mammal Rev 37(2): 81–115.
Ortega, CP (2012) Effects of noise pollution on birds: A brief review of our knowledge. Ornithol Monogr 74: 6–22.
Panetta D, Camarlinghi N (2020) 3D Image Reconstruction for CT and PET: A practical guide with python (1st ed.) (CRC Press).
Ruggero MA, Temchin AN (2002) The roles of the external, middle, and inner ears in determining the bandwidth of hearing. PNAS 99: 13206–13210.
Sadé J, Handrich Y, Bernheim J, Cohen D (2008) Pressure equilibration in the penguin middle ear. Acta Otolaryngol 128(1): 18–21.
Slabbekoorn H, Dooling RJ, Popper AN, Fay RR (2018) Effects of anthropogenic noise on animals. Springer Verlag, New York.
Salas AK, Wilson PS, Fuiman LA (2019a) Predicting pressure sensitivity through ontogeny in larval red drum (*Sciaenops ocellatus*). Proc Mtgs Acoust 37: 010006.
Salas AK, Wilson PS, Fuiman LA. (2019b). Ontogenetic change in predicted acoustic pressure sensitivity in larval red drum (*Sciaenops ocellatus*). J Exp Biol 222: jeb201962.
Schoeman RP, Erbe C, Pavan G, Righini R, Thomas JA (2022) Analysis of soundscapes as an ecological tool. In: Erbe C, Thomas JA (eds) Exploring animal behavior through sound: Volume 1: Methods. Springer International Publishing, Cham, pp. 217–267.
Smith AB, Fischer-McMorrow I, Kolbeinsson Y, Rasmussen M, Shero MR, McElwaine JN, Jones OR, Mooney TA (2023a) Sensitive aerial hearing within a noisy nesting soundscape in a deep-diving seabird, the common murre *Uria aalge*. Mar Ecol Prog Ser 714: 87–104.
Smith AB, Kissling M, Capuano AM, Lewis SB, Mooney TA (2023b) Aerial hearing thresholds and ecoacoustics of a threatened pursuit-diving seabird, the marbled murrelet *Brachyramphus marmoratus*. Endang Species Res 50: 167−179
Smith AB, Kissling M, Rasmussen M, Kolbeinsson Y, Capuano A, Fischer MI, Lewis S, Shero MR, Mooney, TA (2023c) Acoustic sensory ecology of diving alcid seabirds and potential noise impacts. In: Popper AN, Sisneros J, Hawkins AD & Thomsen F(eds), The effects of noise on aquatic life: Principles and practical considerations. Springer.
Southall BL, Bowles A, Ellison W, Finneran J, Gentry R, Greene CJr, Kastak D, Ketten D, Miller J, Nachtigall P, Richardson W, Thomas J, Tyack P (2008) Marine mammal noise exposure criteria: initial scientific recommendations. Bioacoustics 17: 273–275.
Sørensen K, Neumann C, Dähne M, Hansen KA, Wahlberg M. (2020) Gentoo penguins (*Pygoscelis papua*) react to underwater sounds. R Soc Open Sci 26: 7(2): 191988.
Thompson LL, and Pinsky PM (1994) Complex wave number Fourier analysis of the p-version finite element method. Comput Mech 13: 255–275.
Tubelli AA, Zosuls A, Ketten DR, Mountain DC (2018) A model and experimental approach to the middle ear transfer function related to hearing in the humpback whale (*Megaptera novaeangliae*). J Acoust Soc Am 144(2): 525–535.
Tubelli AA, Zosuls A, Ketten DR, Mountain DC (2014) Elastic modulus of cetacean auditory ossicles. Anatom Rec 297(5): 892–900.

Tubelli AA, Zosuls A, Ketten DR, Yamato M, Mountain DC (2012) A prediction of the minke whale (*Balaenoptera acutorostrata*) middle-ear transfer function. J Acoust Soc Am 132(5): 3263–3272.
Urick RJ (1983) Principles of Underwater Sound. McGraw-Hill, New York, pp. 1–423.
Wang X, Gan RZ (2016) 3D finite element model of the chinchilla ear for characterizing middle ear functions. Biomech Model Mechanobiol 15(5): 1263–1277.
Wei C, McCauley RD (2022) Numerical modeling of the impacts of acoustic stimulus on fish otoliths from two directions. J Acoust Soc Am 152(6): 3226–3234.
Wever EG, Herman PN, Simmons JA, Hertzler DR (1969) Hearing in the blackfooted penguin, *Spheniscus demersus*, as represented by the cochlear potentials. Proc Natl Acad Sci USA 63(3): 676–80.

Submitted as draft	22/3/2024
Review completed	7/6/2024
Submitted as revised draft	29/6/2024
Approved by Science Program Leadership Team	23/7/2024
Approved by WAMSI CEO	7/8/2024
Final report	27/8/2024

WESTERN AUSTRALIAN
MARINE SCIENCE
INSTITUTION